EVALUATION OF TURBULENCE MODELS FOR THE PREDICTION OF VORTEX INTERACTION OVER A FIGHTER AIRCRAFT

Michel Visonneau, Emmanuel Guilmineau, Ginevra Rubino

AerospaceEurope Conference2020
BORDEAUX, FRANCE | 25 - 28 FEBRUARY 2020
CEAS Council of European Aerospace Societies
HOSTED BY : 3AF Association Aéronautique et Astronautique de France

EVALUATION OF TURBULENCE MODELS FOR THE PREDICTION OF VORTEX INTERACTION OVER A FIGHTER AIRCRAFT

E. Guilmineau [(1)], M. Visonneau [(1)], G. Rubino [(1)]

[(1)] LHEEA, CNRS UMR 6598, Centrale Nantes, 1 rue de la Noë, BP 92101, 44321 Nantes Cedex 3, France:
Email: emmanuel.guilmineau@ec-nantes.fr
Email: michel.visonneau@ec-nantes.fr
Email: ginevra.rubino@ec-nantes.fr

KEYWORDS: Turbulence models, vortex interaction, aircraft, RANS model, Hybrid RANS-LES model

ABSTRACT:

In the present work, the numerical simulations of flow around a fighter aircraft at several angles of attack are performed with the flow solver ISIS-CFD which is an incompressible unsteady Reynolds-averaged Navier-Stokes method. Three RANS-based turbulence models, as the isotropic k- SST, the non-linear anisotropic EARSM, and the Reynolds stress transport model SSGLRR-ω and one hybrid RANS-LES model, the DDES-SST, are used. All these turbulence models are based on k-ω model. Forces and moments as well as flow field data are compared with experimental measurements. For the RANS-based turbulence models, the results obtained with k-ω SST agree relatively well with the experimental data and it is the better approach for this class of turbulence models. However, the results obtained with DDES-SST are in better agreement with experiments.

1. INTRODUCTION

Aircraft that manoeuvres through large angles of attack (AoA) will experience large regions of flow separation over the wing and fuselage. High AoA aircraft is frequently encountered during landing and take-off phases, and during combat manoeuvring. The separated flow field is characterized by unsteady and strong vortical flow structures that can interact with various components of the aircraft and among themselves. These complicated flow interactions are the primary cause of most flight dynamic instabilities. Some aspects of the vortex-interaction flow physics are not well understood and they are a challenging aspect of the numerical simulation of the flow around aircraft configurations. Recently, an example of the flow simulation of the interaction between the inner and outer vortices of F-16XL aircraft has been published [1].

A low-aspect-ratio multiple-swept wing fuselage configuration is currently studied in the NATO STO AVT-316 task group on “Vortex Interaction Effects Relevant to Military Air Vehicle Performance”. This collaborative research has been built to assess the capability of current CFD (Computational Fluid Dynamics) methods to predict vortex-interaction effects, extend our understanding of vortex-interaction flow physics for these problems trough numerical and physical experimentation.

In this paper, we conducted a numerical simulation of the flow past a military aircraft at Mach number 0.15 and several angles of attack by means of RANS simulations and hybrid RANS-LES simulations. A comparison will be made between the numerical results and experimental data.

2. TEST-CASE

The model aircraft is a triple delta wing configuration with three different consecutive wing sections featuring a varying leading-edge sweep. This model is called NA1 W1 configuration and is shown in Fig. 1. The length of the aircraft is l_{tot} = 1.16 m, the spanwise is $b = 2s$ = 0.8332 m and the size of the wing root is $l_{ref} = c_r$ = 0.8022 m. This model is studied in the framework of the Research Technical Group NATO/AVT-316 and entitled “Vortex Interaction Effects Relevant to Military Air Vehicle Performance” [2-3].

Experiments are conducted in a wind tunnel of the Technical University of Munich for a speed of V_∞ =

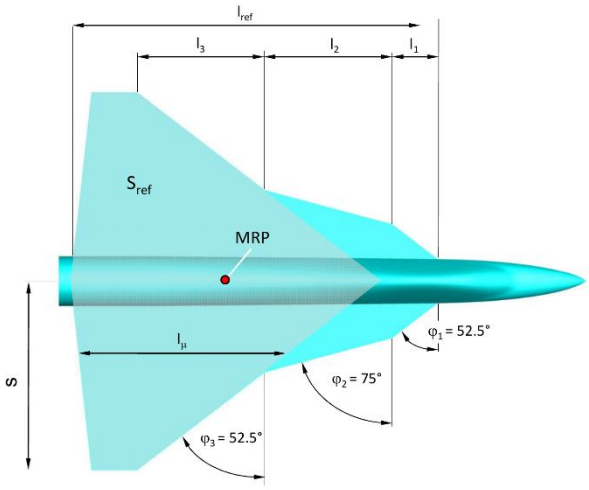

Figure 1. Aircraft model

51.97 m/s, which leads to a Reynolds number, based on l_{ref}, of 2.38 10^6 and a Mach number of 0.15, a value for which is still reasonable to use an incompressible flow solver. Drag, lift and moment are measured at several angles of attack, α, ranging from 4° to 40°. PIV measurements are also conducted at 8°, 16°, 24° and 32° angles of attack. Two angles of sideslip, β, are investigated: 0° and 5° Sixteen cross-sections covering the wing have been chosen where the three velocity components, the longitudinal vorticity and the three normal Reynolds stress components are measured.

In this paper, we only focus on 4 sections at x/c_r = 0.125, x/c_r = 0.475, x/c_r = 0.592 and x/c_r = 0.825 called respectively Slice 1, Slice 2, Slice 3 and Slice 4 and shown in Fig. 2.

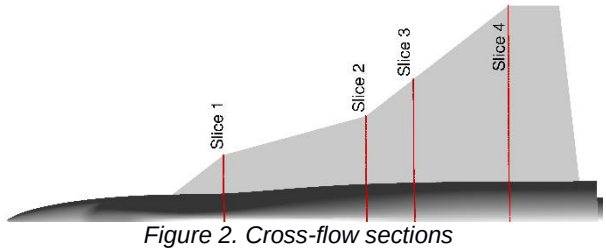

Figure 2. Cross-flow sections

3. ISIS-CFD AT GLANCE

The ISIS-CFD flow solver, developed by Centrale Nantes and CNRS, uses an incompressible Unsteady Reynolds-Averaged Navier-Stokes (URANS) method. The solver is based on a finite volume method to build the spatial discretization of the transport equations. The unstructured discretization is face-based, which means that cells with an arbitrary number of arbitrarily shaped faces are accepted. A second order backward difference scheme is used to discretize time. The solver can simulate both steady and unsteady flows. In the case of turbulent flows, additional transport equations for the variables in the turbulence model are added. All flow variables are stored at the geometric centre of an arbitrary shaped cells. Volume and surface integrals are evaluated with second-order accurate approximations. Numerical fluxes are reconstructed on the mesh faces by linear extrapolation of the integrand from the neighbouring cell centres. The velocity field is obtained from the momentum conservation equations and the pressure field is extracted from the mass conservation constraint or continuity equation, transformed into a pressure-equation. The pressure equation is obtained by the Rhie and Chow interpolation technique [4]. The momentum and pressure equations are solved in a segregated manner as in the SIMPLE coupling procedure [5].

The solver features sophisticated turbulence models: apart from the classical two-equation k-ε and k-ω models, the anisotropic two-equation Explicit Algebraic Reynolds Stress Model (EARSM), as well as Reynolds Stress Transport Models, are available [6-8]. All these turbulence models are RANS models. A Detached Eddy Simulation (DES) approach, based on k-ω model, has been introduced [9]. Recently, some modifications of this formulation proposed by Gritskevich et al. [10] include recalibrated empirical constants in the shielding function for the Delayed Detached Eddy Simulation (DDES) and a simplification of the original Spalart-Allmaras-based formulation for the Improved Delayed Detached Eddy Simulation (IDDES) are implemented, as well.

An anisotropic automatic grid refinement (AGR) procedure based on various flow-related criteria has been developed [11]. Recently, AGR has been coupled with the hybrid RANS-LES approaches [12-13] by using an average-based adaptation procedure to create static mesh topologies based on the main flow features.

4. NUMERICAL SIMULATION SET-UP

For this study, only the symmetric freestream conditions (β = 0°) are investigated and the turbulence models used are: k-ω SST, EARSM, SSGLRR-ω for the RANS models and DDES-SST for the hybrid RANS-LES modelisation.

The average-based mesh adaptation procedure is also used, choosing as the refinement criterion the flux component Hessian. As the flow depends on the turbulence model, the number of cells varies depending on the turbulence model and the angle of attack α. For the angles of attack investigated, from 8° to 32°, the number of cells varies from 31.7 million to 74.2. The meshes are generated using Hexpress™, an automatic unstructured mesh generator. This software generates meshes containing only hexahedrals. For the aircraft and the sting, no-slip boundary condition is imposed and wall normal resolution with y^+, below 1. Fig. 3 presents a view of mesh at Slice 3 for AoA 8° while Fig.4 shows the mesh in the Slice 3 for AoA 24°.

5. RESULTS

5.1. Integral data

Fig. 5 presents the evolution of the drag and lift coefficients and the pitching moment coefficient versus the angle of attack. With the k-ω SST the results are in good agreement with the experimental data, except for the angle of attack α = 32° which corresponds to the stall angle where all forces predicted by the numerical simulations are overestimated.

The variation of the shape of the pitching moment curve around the angle of attack 12° is well

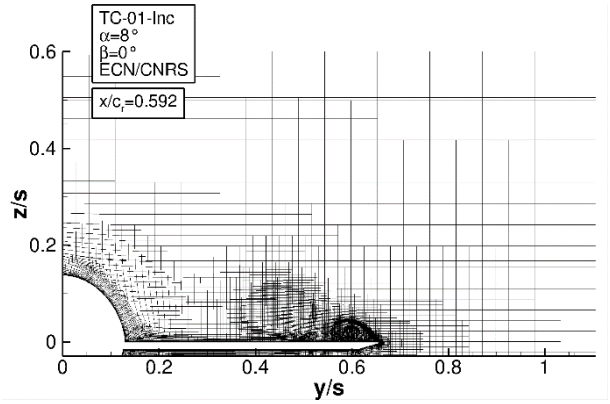

Figure 3. α = 8°: View of the mesh in Slice 3

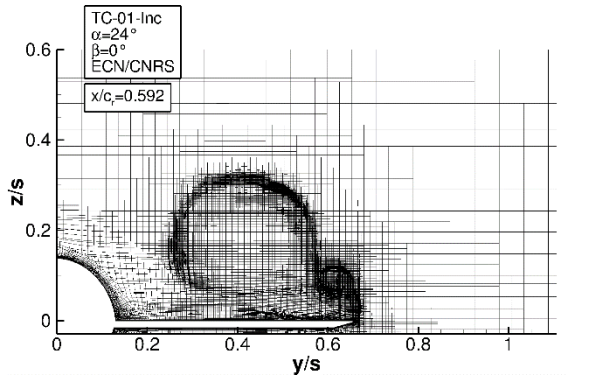

Figure 4. α = 24°: View of the mesh in Slice 3

predicted with the k-ω SST turbulence model. This change is due to the apparition of the negative velocity in the core of the vortex, as shown in Fig. 6 where the vortex structures for the angle of attack around 12° are presented. These figures show the isosurface of the non-dimensional second invariant (Q* = 50), the blue translucent surface, and the isosurface of the first component of the velocity, the red surface. The flow is characterised by two primary leading-edge vortices. The first vortex develops at the most inboard wing section and is called inboard vortex (IBV). The second vortex develops at the kink from the highly swept to the medium swept wing section at x/c_r = 0.475 and is called midboard vortex (MBV) For an angle of attack below of 12°, the two vortices do not interact amongst themselves. From AoA 12°, a negative velocity appears in the core of the vortex, indicating reverse flow and vortex-vortex interaction, as well.

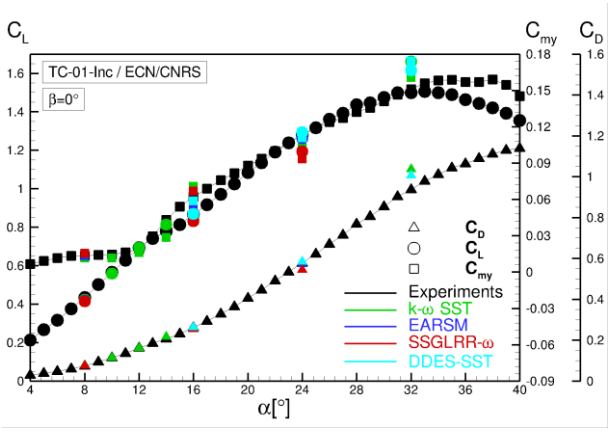

Figure 5. Comparison of aerodynamic coefficients, drag coefficient, lift coefficient and pitching moment coefficient, versus the angle of attack α

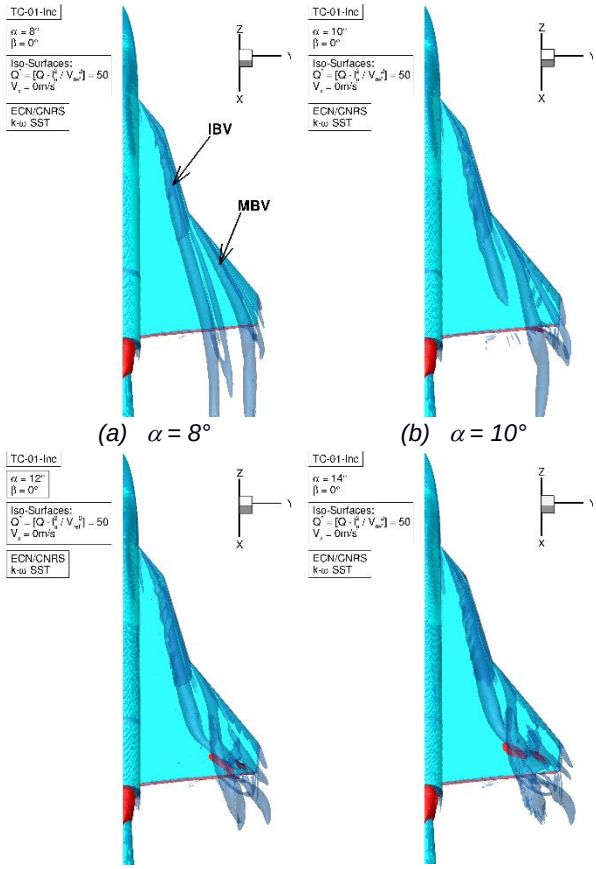

Figure 6. Vortical structures obtained with the k-ω SST turbulence model for the angles of attack 8°, 10°, 12° and 14°

With EARSM turbulence model, the forces are well predicted for all angles of attack, but the pitching moment is in less good agreement with the experimental data as the angle of attack increases. With the Reynolds stress model, SSGLRR-ω, the agreement with the experimental data is less good compared to other turbulence models. The hybrid RANS-LES model, DDES, ensures a very good agreement with the experimental data, except for the angle of attack α = 32°. For angles of attack below 32°, the error with the experimental data is below 1.2% for the forces and 5.5% for the moment.

5.2. Angle of attack α = 8°

Fig. 7 presents the vortex structures obtained with different turbulence models for the angle of attack α = 8°. All numerical simulations predict the same flow. The two primary vortices, the IBV and the MBV, do not show an interaction. Each vortex

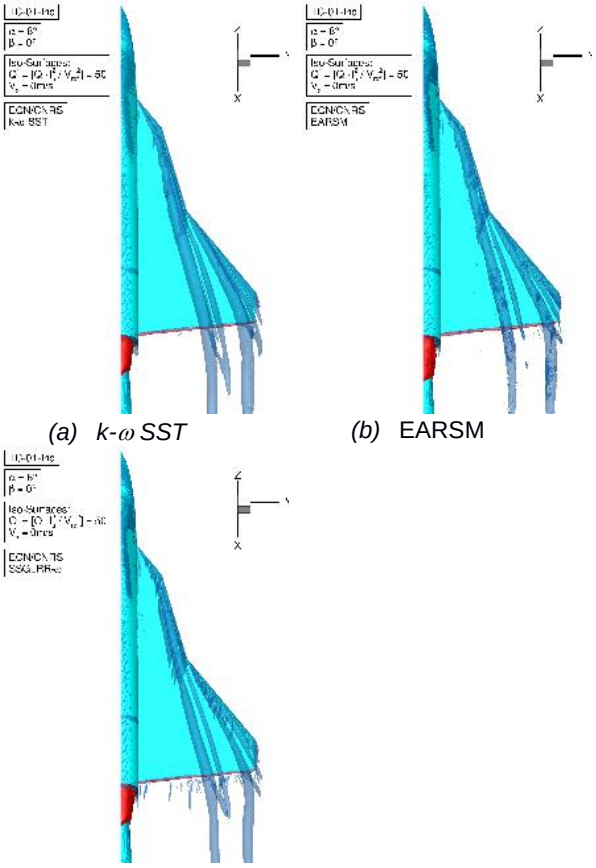

(a) k-ω SST (b) EARSM

(c) SSGLRR-ω

Figure 7. α = 8° - Vortical structures°

exhibits a secondary structure.

Figs. 8 and 9 present the distribution of the axial vorticity for the Slice 2 and 3, respectively. For each figure, a compassion between all numerical results and the experimental data is presented. We observe a decreasing of the axial vorticity in the IBV which indicates the bursting of this vortex. In the slice 2, see Fig. 8, the axial vorticity in the core of the vortex is overestimated by all numerical simulations, particularly with SSGLRR-ω turbulence model. In this slice, the secondary structure of the IBV, indicated by the negative axial velocity, is present.

At Slice 3, see Fig. 9, the MBV is present. Here too, the results show that the vorticity in the core of the core is overestimated in comparison with the experimental data. At Slice 4 (figure not presented), the level of the axial vorticity decreases in the core of the IBV.

Fig. 10 shows the turbulent kinetic energy, TKE, at Slice 3. In the experiments, the level of TKE is high the core of the IBV and MBV while with the k-ω SST and EARSM models, this level is very low. The level of TKE in the IBV predicted by SSGLRR-ω model is higher compared to the other turbulence models. However, it is still lower than the experimental value.

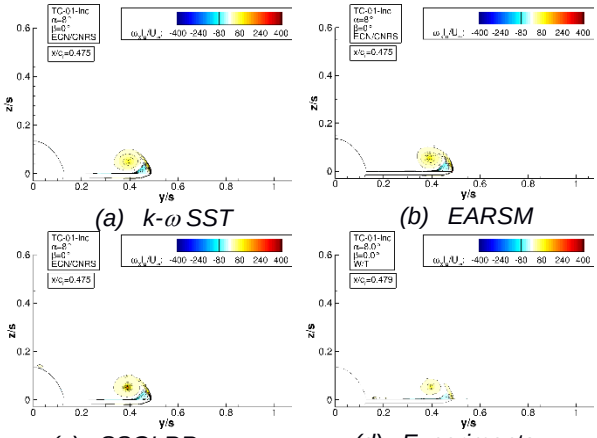

(a) k-ω SST (b) EARSM

(c) SSGLRR-ω (d) Experiments

Figure 8. α = 8° - Axial vorticity in Slice 2, x/c$_r$ = 0.475

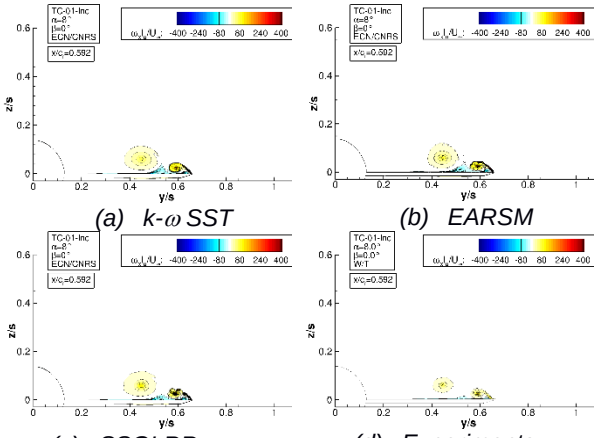

(a) k-ω SST (b) EARSM

(c) SSGLRR-ω (d) Experiments

Figure 9. α = 8° - Axial vorticity in Slice 3, x/c$_r$ = 0.592

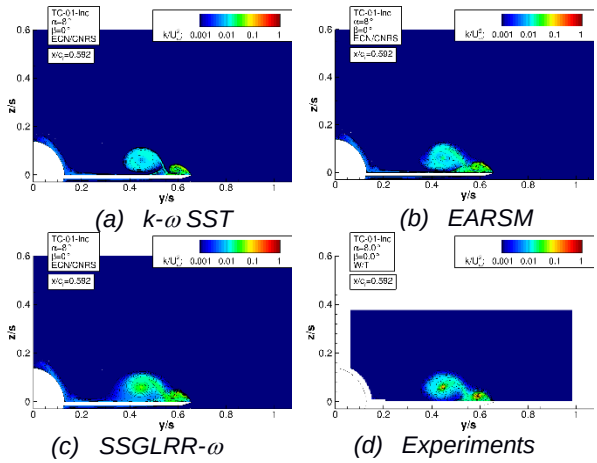

(a) k-ω SST (b) EARSM

(c) SSGLRR-ω (d) Experiments

Figure 10. α = 8° - Turbulent kinetic energy in Slice 3, x/c$_r$ = 0.592

5.3. Angle of attack α = 16°

For the angle of attack α = 16°, see Fig. 11, the vortices interact and an area with a negative velocity is present which means a bursting of the vortex. However, all turbulence models do not predict this negative velocity zone, see the results obtained with

the EARSM turbulence model. It is observed that the MBV moves towards the fuselage of the aircraft. The size of the vortices predicted with the DDES-SST model is smaller than the size of those predicted with a RANS turbulence model. The EARSM turbulence model is the only model which not predict a reverse flow.

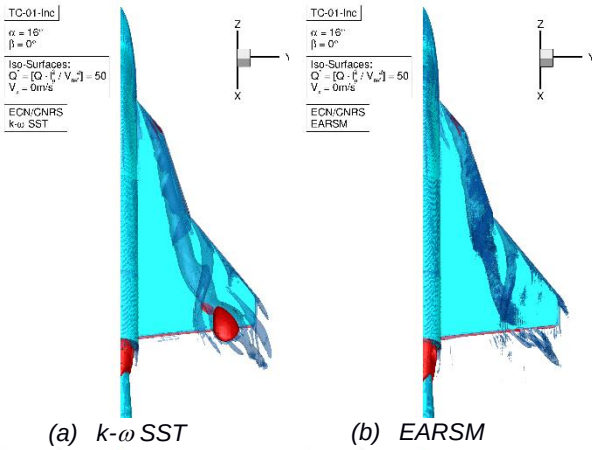

(a) *k-ω SST* (b) *EARSM*

(c) SSGLRR-ω (d) DDES-SST

Figure 11. $\alpha = 16°$ - Vortical structures

Figure 12 presents the axial velocity in the Slice 2, $x/c_r = 0.475$. This figure presents a comparison between all numerical simulations and the experimental data. With the EARSM turbulence model, a low velocity in the core of the IBV is observed while it is not the case in the experiments. The result obtained with the DDES-SST model is in very good agreement with the experimental data.

Figure 13 presents the axial velocity in the Slice 3, $x/c_r = 0.592$. With the EARSM turbulence model, the area where the velocity is low in the core of the vortex is higher than that observed in the experiments. This area with a low velocity is observed in the SSGLRR-ω results, however the velocity is not low enough. With k-ω SST, this area does not exist. The hybrid RANS-LES model DDES-SST, predicts again the best result in agreement with the experimental data.

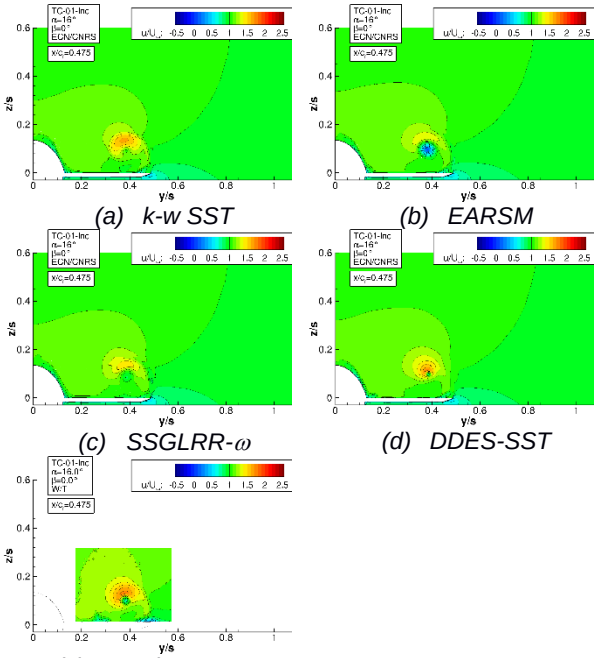

(a) *k-w SST* (b) *EARSM*

(c) *SSGLRR-ω* (d) *DDES-SST*

(e) *Experiments*

Figure 12. $\alpha = 16°$ - Axial velocity in Slice 2, $x/c_r = 0.475$

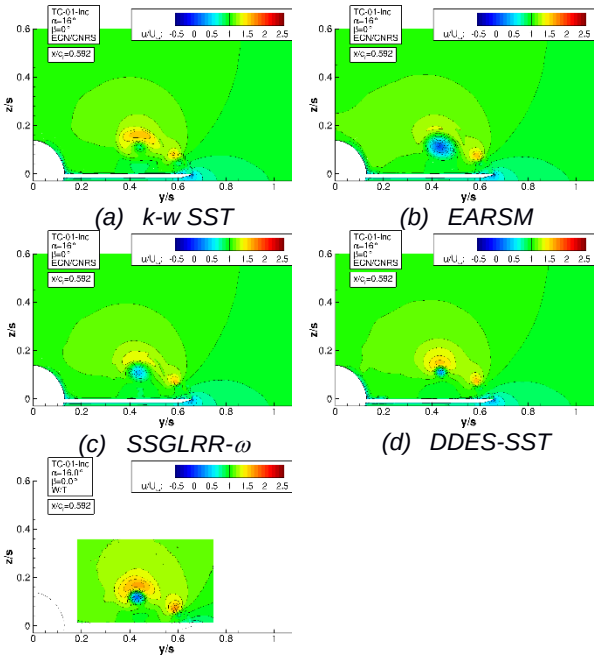

(a) *k-w SST* (b) *EARSM*

(c) *SSGLRR-ω* (d) *DDES-SST*

(e) *Experiments*

Figure 13. $\alpha = 16°$ - Axial velocity in Slice 3, $x/c_r = 0.592$

The axial vorticity at Slice 3 is presented in Fig. 14. The vorticity in the core of the MBV is very high in experiments. SSGLRR-ω overpredicts this level, while with the k-ω SST turbulence model the level is too low. With the other turbulence models, the level is in agreement with the experimental data. For the vorticity in the core of the IBV, only the hybrid RANS-LES model DDES- SST predicts the correct level of the axial vorticity.

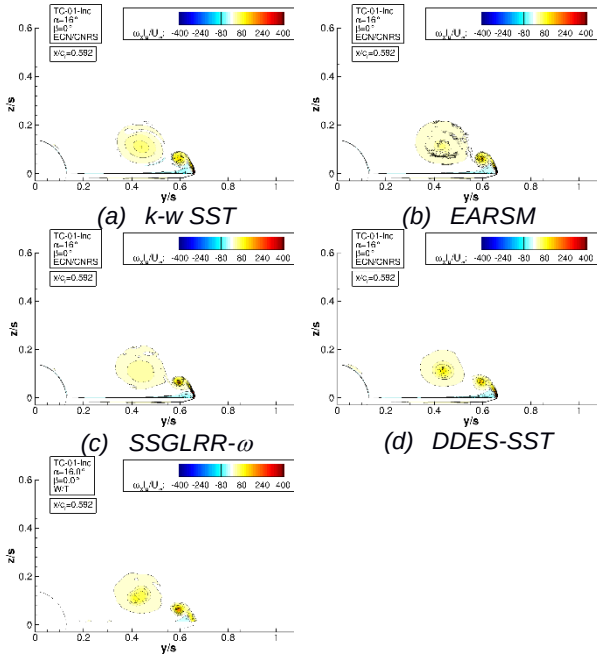

Figure 14. α = 16° - Axial vorticity in Slice 3, x/c_r = 0.592

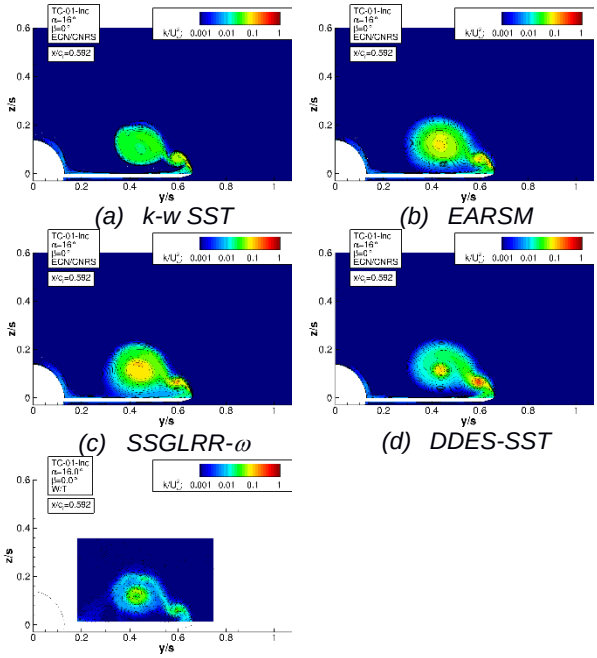

Figure 15. α = 16° - Turbulent kinetic energy in Slice 3, x/c_r = 0.592

The level of TKE in the core of the IBV and MBV is overestimated by all numerical simulations in comparison with the experimental data, see Fig.15. With the k-ω SST turbulence model, the level is very homogeneous in the IBV, contrary to the experiments. With the DDES-SST model, the high level is reached in the core of both vortices. This trend has already been observed in the numerical simulation of a vortex emanating from the sonar dome of a US Navy frigate at static drift [14].

5.4. Angle of attack α = 24°

With the angle of attack α = 24°, see Fig. 16, reverse flow is predicted by all turbulence models. The reverse flow starts at the beginning of the wing, expect with the SSGLRR-ω model where it is located at the bursting. At this AoA, a third vortex exists. At the beginning this vortex follows the fuselage and at the middle of the wing it moves towards the tip of the wing. With EARSM turbulence model, this vortex is very short and it disappears as it leaves the fuselage. In the SSGLRR-ω results, this vortex disappears when the IBV and MBV burst.

Fig. 17 presents the axial velocity in the slice 2, x/c_r = 0.475. In the experiments, the velocity is negative in the core of the IBV vortex and an area with a velocity equal to the upstream velocity, located at the top of the IBV, is present. This characteristic is well predicted with the DDES turbulence model.

With the EARSM and SSGLRR-ω turbulence models, this area is not predicted because of the bursting carried out before this slice.

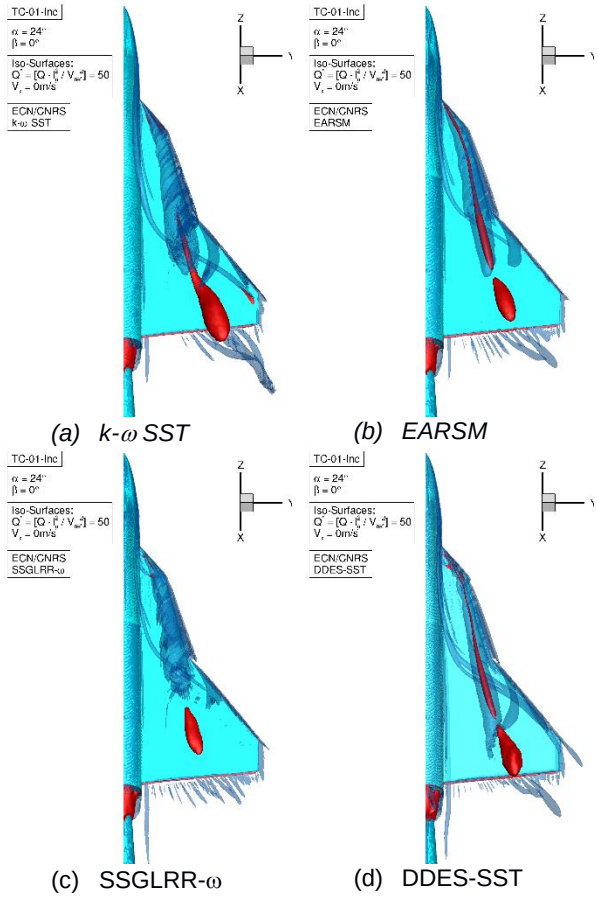

Figure 16. α = 24° - Vortical structures

Fig. 18 presents the axial velocity at Slice 3, x/c_r = 0.592. The presence of the third vortex is also visible at this slice. In the experiments, the level of

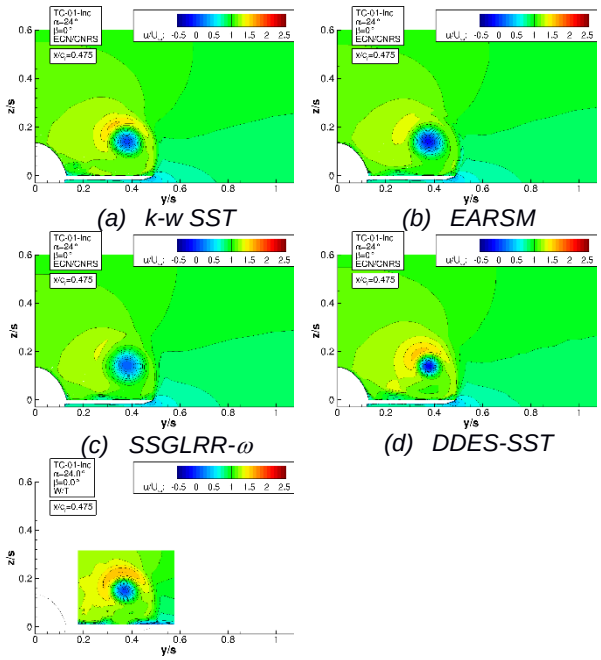

Figure 17. α = 24° - Axial velocity in Slice 2, x/c$_r$ = 0.475

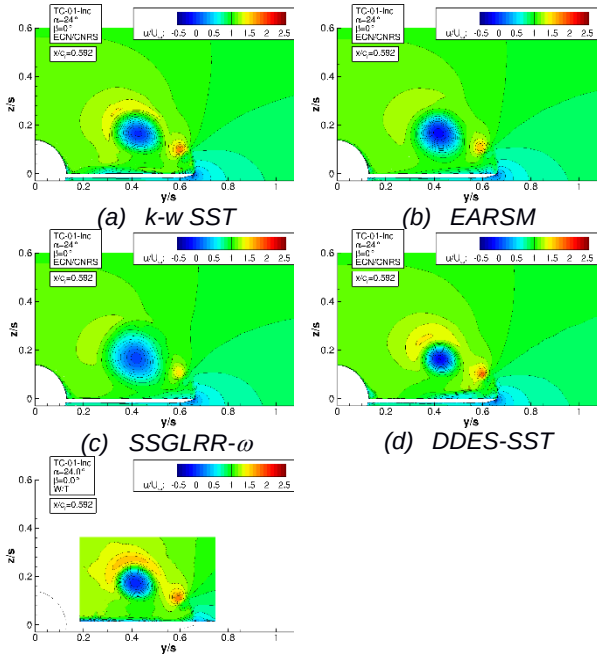

Figure 18. α = 24° - Axial velocity in Slice 3, x/c$_r$ = 0.592

velocity in the core of this very high which is only predicted.

by the k-ω SST and DDES-SST turbulence models. The size of the IBV predicted with the DDES-SST model is in very good agreement with the experimental data.

The distribution the turbulent kinetic energy in the same slice is presented in Fig. 19. In the experiments, when we move from the core of the vortex in the radial direction, the level of TKE increases and decreases. This behaviour is due to the interaction of the IBV and the MBV. The k-ω SST turbulence model is the only one to predict this behaviour.

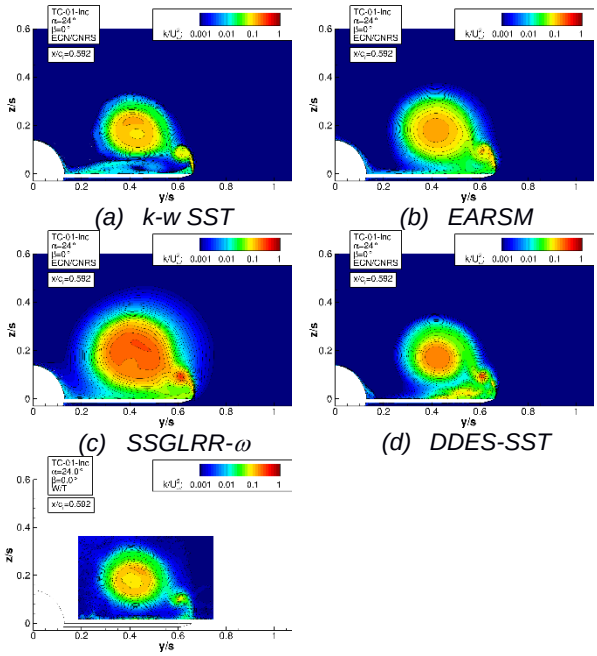

Figure 19. α = 24° - Turbulent kinetic energy in Slice 3, x/c$_r$ = 0.592

In Slice 4, x/c$_r$ = 0.825, the bursting of the IBV and the MBV is done and we observe a very high level of TKE, see Fig. 20. All numerical simulations predict this high level of TKE. However, only the k-ω SST and the DDES model give the correct level of TKE. The shape of the distribution of the turbulent kinetic energy predicted with the DDES model is in very good agreement with the experimental data.

5.5. Angle of attack α = 32°

For the angle of attack, α = 32°, the reverse flow is again present, see Fig. 21. Two other vortices exist along the fuselage and as for the previous AoA, these structures move away from the fuselage towards the tip of the wing. The vortex interaction is very similar to that of the previous AoA. A reverse flow is predicted at the leading edge of the wing.

A comparison of the axial velocity at Slice 2, *x/c$_r$* = 0.475, is presented in Fig. 22. The area with a low velocity is larger in the measurements than in the numerical simulations. With the hybrid RANS-LES model, this area is positioned lower.

A same comparison but at Slice 3, *x/c$_r$* = 0.592, is presented in Fig. 23. With the numerical simulations, we observe an area where the axial velocity is high, and particularly with the k-ω SST

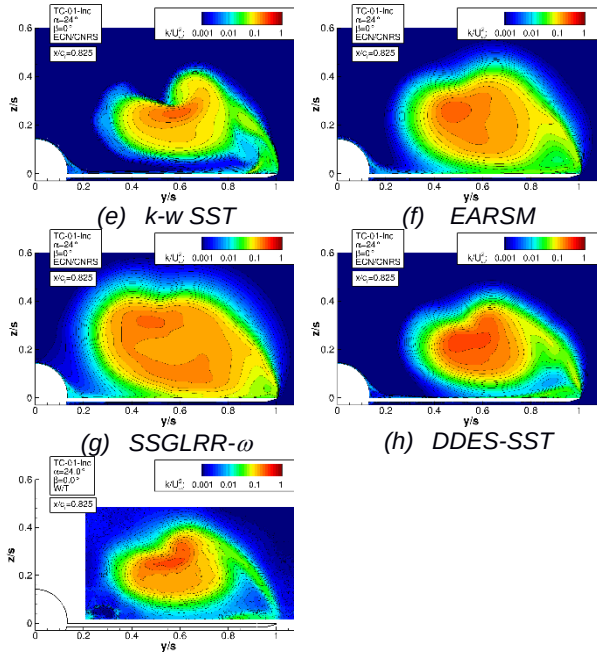

(e) k-w SST (f) EARSM

(g) SSGLRR-ω (h) DDES-SST

(e) Experiments

Figure 20. α = 24° - Turbulent kinetic energy in Slice 4, x/c$_r$ = 0.825

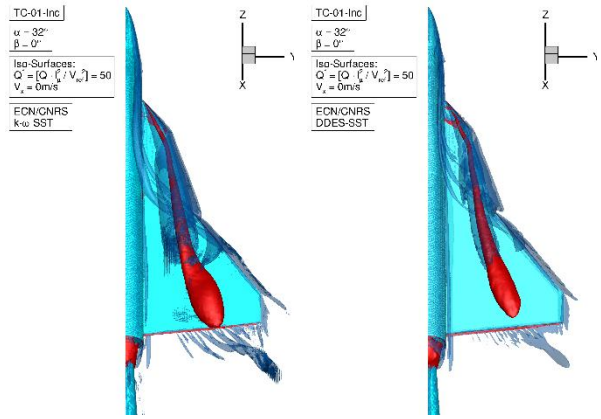

(a) k-ω SST (b) DDES-SST

Figure 21. α = 32° - Vortical structures

turbulence model. This area with high velocity is not present in the experiments. Numerically, this area is probably due to the presence of the two other vortices generated close to the fuselage.

If we compare the turbulent kinetic energy distribution in the same slice, see Fig. 24, we notice that the DDES model overestimates the TKE in the core of the vortex. The level of TKE for the third vortex is well predicted and in agreement with the experimental data. With the k-ω SST model, this level of TKE in the third vortex is very low.

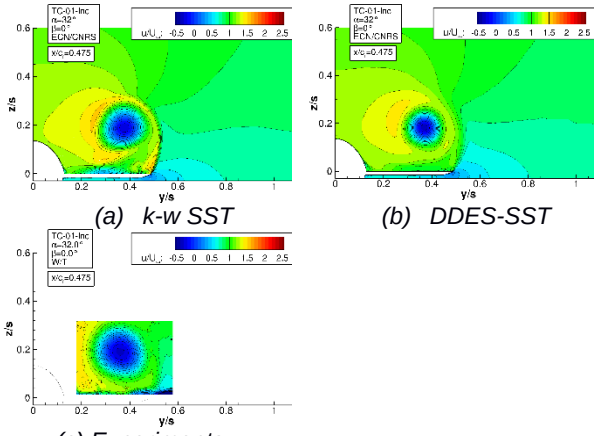

(a) k-w SST (b) DDES-SST

(c) Experiments

Figure 22. α = 32° - Axial velocity in Slice 2, x/c$_r$ = 0.475

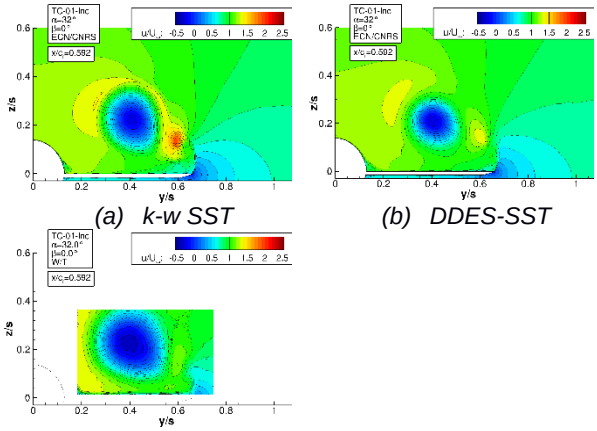

(a) k-w SST (b) DDES-SST

(c) Experiments

Figure 23. α = 32° - Axial velocity in Slice 3, x/c$_r$ = 0.592

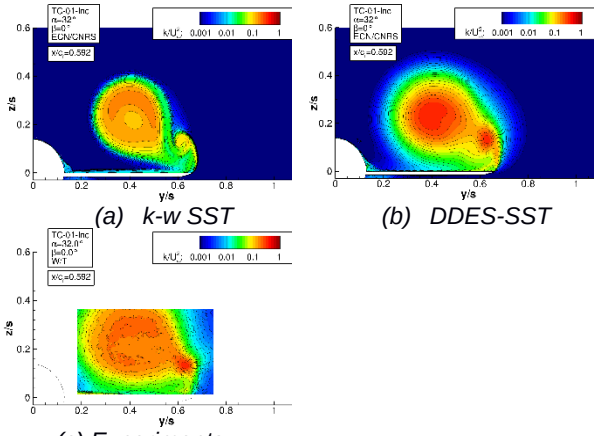

(a) k-w SST (b) DDES-SST

(c) Experiments

Figure 24. α = 32° - Turbulent kinetic energy in Slice 3, x/c$_r$ = 0.592

6. CONCLUSIONS

In this paper, a study of the flow around a military aircraft at several angles of attack has been presented. Numerical simulations were run using the automatic grid refinement, a specificity of the flow solver ISIS-CFD. The numerical results obtained with two linear isotropic turbulence models, k-ω SST and EARSM, a Reynolds stress

transport model, SSGLRR-ω, and a hybrid RANS-LES model, the DDES-SST, are compared to experimental data.

For the aerodynamic coefficients, the hybrid RANS-LES model and the k-w SST results are in very good agreement with the experimental data. For the highest angle of attack, α = 32°, the agreement is less good.

For the comparison of the flow quantities, axial velocity, axial vorticity, DDES results are in good agreement with the measurements. However, the level of the turbulent kinetic energy in the core of the vortex is overestimated.

The next steps are to investigate the influence of the turbulence models with a sideslip angle of 5° and then the evaluation of the impact of the geometry. The next geometry will be a configuration with a double delta wing with two different consecutive wing sections of varying leading-edge sweeps.

Acknowledgements

The computations were performed using HPC resources from GENCI (Grand Equipement National de Calcul Intensif) (Grant-A0042A00129, Grant-A0062A00129) which is gratefully acknowledged. The experimental data were provided in the framework of the NATO-STO task group AVT-316 by Airbus Defence and Space (Aerodynamic Design, TEAGA-TL6) and the Technical University of Munich (Chair of Aerodynamics and Fluid Mechanics, TUM-AER).

REFERENCES

1. Boelens, O.J., Badcock, K.J., Elmilgui, A., Abdol-Hamid, K.S. & Massey, S.J. (2009). Comparison of Measured and Block Structured Results for the F-16XL Aircraft. Journal of Aircraft, **46**(2), 377-384.

2. Hitzel, S.M., Winkler, A. & Hövelmann A. (2019). Vortex Flow Aerodynamic Challenges in the Design Space for Future Fighter Aircraft. In: Dillmann A., Heller G., Krämer E., Wagner C., Tropea C., Jakirlić S. (eds) New Results in Numerical and Experimental Fluid Mechanics XII. DGLR 2018. *Notes on Numerical Fluid Mechanics and Multidisciplinary Design*, **142**, 297-306.

3. Pfnür, S. & Breitsamter, C. (2019). Leading-Edge Vortex Interactions at a Generic Multiple Swept_Wing Aircraft Configuration. Accepted at *Journal of Aircraft*.

4. Rhie, C.M. & Chow W.L. (1983). A Numerical Study of the Turbulent Flow past an Isolated Aerofoil with Trailing Edge Separation, *AIAA Journal* **17**(11), 1525-1532.

5. Issa R.I. (1986). Solution of the Implicitly Discretised Fluid Flow Equations by Operator Splitting. *Journal of Computational Phyics* **62**(1), 40-65.

6. Duvigneau, R. Visonneau, M. & Deng, G.B. (2003). On the Role Played by Turbulence Closures in Hull Ship Optimization at Model and Full Scale. *Journal of Marine Science and Technology* **8**, 11-25.

7. Deng, G.B. & Visonneau, M. (1999). Comparison of Explicit Algebraic Stress Models and Second-Order Turbulence Closures for Steady Flow Around Ships. In 7th International Conference on Numerical Ship Hydrodynamics, Nantes, France.

8. Cecora, R.-D., Radespiel, R., Elsfeld, B. & Probst, A. (2015). Differential Reynolds-Stress Modeling for Aeronautics. *AIAA Journal* **53**(3), 739-755.

9. Guilmineau, E., Deng, G.B. & Wackers, J. (2011). Numerical Simulation with a DES Approach for Automotive Flows. *Journal of Fluids and Structures* **27**(5-6), 807-816.

10. Gritskevich, M.S. Garbaruk, A.V., Schütze, J. & Menter F.R. (2012). Development of DDES and IDDES Forumlations for the k-w Shear Stress Transport Model, *Flow, Turbulence and Combustion* **88**(3), 431-449.

11. Wackers, J., Deng, G.B., Guilmineau, E., Leroyer, A., Queutey, P. & Visonneau, M. (2014). Combined Refinement Criteria for Anisotropic Grid Refinement in Free-Surface Flow Simulations. *Computers & Fluids*, **92**, 209-222.

12. Mozaffari, S., Visonneau, M. & Wackers, J. (2019). Average-based Adaptive Grid Refinement in Hybrid LES, In Direct and Large Eddy Simulation 12 (DLES12), Madrid, Spain.

13. Mozaffari, S. (2020). Adaptive Grid Refinement for Hybrid RANS/LES. PhD Centrale Nantes.

14. Visonneau, M., Guilmineau, E. and Rubino, G. (2018). Computational Analysis of the Flow around a Surface Combatant at 10° Static Drfit and Dynamic Sway Conditions. In 32nd Symposium on Naval Hydrodynamics, Hamburg, Germany.